remote sensing

MDPI

Article

Mapping Evapotranspiration Patterns in the Desert-Oasis Ecotone Using UAV-Based Thermal Infrared Imagery with a Three-Temperature Model

Siying Li [1,2], Yuhua Xing [1,3], Dapeng Zhang [1,2] and Pei Wang [1,2,*]

[1] State Key Laboratory of Earth Surface Processes and Disaster Risk Reduction, Faculty of Geographical Science, Beijing Normal University, Beijing 100875, China; 202221051158@mail.bnu.edu.cn (S.L.); 202121051112@mail.bnu.edu.cn (Y.X.); 202121051139@mail.bnu.edu.cn (D.Z.)
[2] School of Natural Resources, Faculty of Geographical Science, Beijing Normal University, Beijing 100875, China
[3] Institute of Ecology, College of Urban and Environmental Sciences, Peking University, Beijing 100091, China
* Correspondence: peiwang@bnu.edu.cn

Highlights

What are the main findings?

- A high-resolution evapotranspiration (ET) mapping framework was developed by integrating unmanned aerial vehicle (UAV)-based thermal infrared imagery with the three-temperature (3T) model, successfully capturing the sharp spatial gradient of ET across the desert-oasis ecotone (cropland > shelterbelt > desert).
- The 3T model demonstrated high reliability, with spatial validation against Surface Energy Balance Algorithm for Land (SEBAL) model yielding R^2 = 0.90–0.95 and RMSE = 0.22–0.43 mm d^{-1}, and point-scale validation against a two-source model showing a mean absolute error of 0.38 mm d^{-1}.

What are the implications of the main findings?

- This study provides a practical, high-resolution technical solution for ET monitoring in heterogeneous ecological transition zones, overcoming the limitations of coarse satellite data and sparse ground stations.
- The generated meter-scale ET maps offer direct, quantifiable data to support water-smart ecological management, such as "greening based on water capacity", and the optimization of vegetation configuration in arid regions.

Abstract

Evapotranspiration (ET) estimation in desert-oasis ecotones remains challenging due to sparse meteorological observations and the coarse spatial resolution of satellite remote sensing, which limit the ability to resolve highly heterogeneous surface conditions. To address this issue, this study develops a high-resolution ET estimation framework by integrating unmanned aerial vehicle (UAV)-based thermal infrared remote sensing with a three-temperature (3T) model in the Hexi Corridor. UAV-derived land surface temperature (LST) at meter-scale resolution, together with meteorological and vegetation data, was used to drive the model and generate high-resolution ET maps. The model's performance was validated spatially against the Surface Energy Balance Algorithm for Land (SEBAL) model and at the point-scale against a two-source model. The results show that: (1) The 3T model effectively captured the spatial gradient of decreasing ET from cropland (3–10.69 mm d^{-1}), through shelterbelts (3–6 mm d^{-1}), to desert areas (<3 mm d^{-1}). (2) Spatial validation against the SEBAL model was conducted using stratified pixel-wise comparisons across

Check for updates

Academic Editor: Nicola Montaldo

Received: 25 May 2026
Revised: 1 July 2026
Accepted: 2 July 2026
Published: 7 July 2026

Copyright: © 2026 by the authors. Licensee MDPI, Basel, Switzerland. This article is an open access article distributed under the terms and conditions of the Creative Commons Attribution (CC BY) license.

four land-cover types over 14 UAV transects, showing strong agreement (R^2 = 0.90–0.95; RMSE = 0.22–0.43 mm d^{-1}). The model achieved highest accuracy in cropland (R^2 = 0.92; RMSE = 0.24 mm d^{-1}), with slight overestimation in shelterbelts. (3) Point-scale validation against the two-source model yielded an MAE of 0.38 mm d^{-1}. This study demonstrates the effectiveness of combining UAV thermal infrared data with the 3T model for high-resolution ET simulation in complex ecological transition zones, offering a promising technical approach for ecohydrological monitoring and water resource assessment in arid regions.

Keywords: evapotranspiration; UAV thermal infrared; three-temperature model; desert-oasis ecotone; high-resolution mapping; model validation

1. Introduction

Evapotranspiration (ET) is a key hydrological process linking the soil–plant–atmosphere continuum and represents the dominant component of the water balance in arid regions [1,2]. The desert-oasis ecotone serves as a critical ecological buffer for windbreak and sand fixation, where ecosystem functioning is strongly constrained by limited water availability [3,4]. Accurate characterization of ET is therefore essential for assessing ecological water consumption, vegetation sustainability, and water resource management in these fragile transition zones [5–7]. In the Hexi Corridor, increasing competition for limited water resources has intensified ecological water stress [8], making accurate ET estimation particularly important for vegetation management and ecological restoration [9–11]. However, accurately monitoring ET in desert-oasis ecotones remains challenging because of the pronounced spatial heterogeneity of vegetation and bare soil.

Evapotranspiration has been widely estimated using multiple approaches, such as ground-based measurements, numerical modeling, remote sensing and machine learning methods [12–15]. Nevertheless, accurately monitoring ET in the desert-oasis ecotones remains challenging due to the strong spatial heterogeneity and insufficient in situ observations. Ground-based methods (e.g., eddy covariance systems and lysimeters) provide point-scale measurements but lack spatial representativeness, making them unsuitable for large-scale and long-term analyses [16,17]. Remote sensing-based ET products (e.g., MOD16) and model simulations can partially overcome these limitations [18,19]. However, their spatial resolution is often coarser than the typical width of the ecotones, resulting in mixed pixels and limited capability to distinguish vegetation transpiration from soil evaporation [19]. In addition, desert-oasis ecotones are subject to frequent human activities, such as the installation of engineering sand barriers, straw checkerboard barriers, and afforestation [20]. These interventions create strong environmental gradients, posing significant challenges for characterizing spatial patterns of water consumption. Although machine learning methods have recently shown promising performance in ET estimation, they generally rely on large amounts of training data and lack explicit physical interpretability, limiting their transferability to data-scarce desert-oasis ecotones [21,22]. Consequently, there is an urgent need for novel monitoring methods that combine high spatial resolution with robust physical mechanisms to better characterize water consumption patterns across heterogeneous ecological transition zones.

Recently, unmanned aerial vehicle (UAV) remote sensing has emerged as a promising tool to bridge the scale gap between ground observations and satellite remote sensing, owing to its high spatiotemporal resolution and operational flexibility [23–25]. UAVs equipped with thermal infrared sensors can acquire land surface temperature (LST) data

at submeter-to-meter resolutions, providing critical input for energy balance-based ET models. The three-temperature (3T) model is a physically based ET estimation model that cleverly circumvents the difficult computation of aerodynamic resistance by introducing a non-evaporating "reference surface" showing strong potential for application in arid and semi-arid regions [26–28]. Thermal infrared UAV observations combined with 3T models have been increasingly applied to quantify patch-scale surface temperature and evapotranspiration in a range of ecosystems, including wetlands, urban areas, and agricultural ecosystems [29–31]. Nevertheless, research on coupling high-resolution UAV thermal infrared data with the 3T model for ET mapping in complex, narrow ecological transition zones, like the desert-oasis ecotone, remains scarce.

To address these issues, this study develops an UAV thermal infrared-driven evapotranspiration estimation framework based on the 3T model, aiming to resolve fine-scale ET heterogeneity in desert-oasis ecotones. Specifically, the study investigates (1) the extent to which the UAV-driven 3T model captures spatial variability of evapotranspiration across heterogeneous land-cover types, and (2) the performance consistency of the model under different surface conditions. The remainder of this paper is organized as follows. Section 2 describes the study area, UAV thermal infrared data acquisition, and the 3T model implementation. Section 3 presents ET results, validation and land-cover comparisons. Section 4 discusses applicability, uncertainty, and implications for vegetation optimization. Section 5 concludes the study.

2. Materials and Methods

2.1. Study Area

The study was conducted in the central Hexi Corridor, which experiences a typical temperate continental arid climate (Figure 1). Multiple representative desert-oasis ecotone transects (HX1–HX15) were selected in Wuwei and Zhangye, Gansu Province, China (Table 1). These sites exhibit a clear landscape gradient: from irrigated cropland through shelterbelts (dominated by *Elaeagnus angustifolia* and *Populus* spp.), transitioning to desert shrubland (featuring drought-tolerant species like *Nitraria tangutorum* and *Haloxylon ammodendron*), and finally to active sand dunes. The region receives less than 200 mm of annual precipitation but has extremely high evaporation potential, leading to acute water resource constraints. The depth to groundwater generally ranges from 4 to 10 m. The dominant soil types are Aripsamments and Calciorthids. Surface soils are mainly sand and sandy loam, characterized by a loose structure and low organic matter content [20].

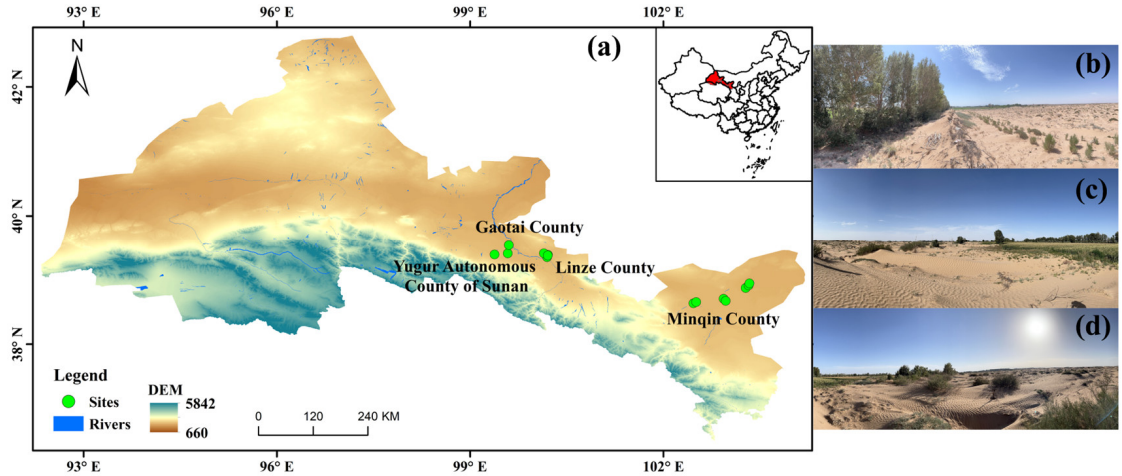


Figure 1. (**a**) Study area. (**b**–**d**) Landscapes of typical desert-oasis ecotones in the Hexi Corridor.

Table 1. Locations of desert-oasis ecotones [1].

Site	Coordinates	Location
HX1	102.468E, 38.634N	Minqin County, Wuwei
HX3	102.509E, 38.653N	
HX4	103.278E, 38.871N	
HX5	103.324E, 38.910N	
HX6	102.934E, 38.704N	
HX7	102.968E, 38.670N	
HX8	103.337E, 38.943N	
HX9	100.210E, 39.385N	Linze County, Zhangye
HX10	100.195E, 39.350N	
HX11	100.146E, 39.410N	
HX12	100.207E, 39.376N	
HX13	99.585E, 39.408N	Gaotai County, Zhangye
HX14	99.602E, 39.538N	
HX15	99.379E, 39.392N	Sunan Yugur Autonomous County, Zhangye

[1] HX2 was excluded due to field data quality issues during sampling and was not included in subsequent analyses.

2.2. UAV Thermal Infrared Data Acquisition and Remote Sensing Time Serial Data

Aerial surveys were conducted during the growing season in July 2023 using a DJI Matrice 300 RTK UAV (Shenzhen, China) equipped with a WIRIS Pro dual-camera thermal infrared imager (Workswell, Prague, Czechia). The WIRIS Pro thermal infrared sensor operates in the spectral range of 7.5–13.5 μm and has a detector resolution of 640 × 512 pixels. Flights were conducted at an altitude of 50–60 m above ground level. Thermal infrared imagery was acquired and processed to generate land surface temperature (LST) products with a ground sampling distance (GSD) of approximately 0.1 m per pixel. Radiometric calibration and temperature retrieval for the thermal imagery were performed according to the sensor manual. In situ ground surface temperatures were measured using a handheld infrared thermometer for representative land-cover types, and were used to cross-validate UAV-derived temperature estimates. Agisoft Metashape (Version 1.8.3) and ENVI (Version 5.6) were used for image stitching, orthorectification, and generation of a digital elevation model (DEM) and LST products (Figure 2).

Due to the limited temporal coverage of data obtained from UAV-based data, which is insufficient for studying long-term dynamic changes in evapotranspiration processes, this study therefore employs remote sensing evapotranspiration products to evaluate the temporal characteristics of evapotranspiration in the desert-oasis ecotones from 2022 to 2024. As the desert-oasis ecotone is located at the edge of an arid region and covers a relatively small area, most existing evapotranspiration products are unable to capture its evapotranspiration characteristics. Consequently, this study conducts a comparative analysis of various mainstream remote sensing evapotranspiration products and ultimately selects the MODIS indirectly derived evapotranspiration product (MOD16A2GF.061: Terra Net Evapotranspiration Gap-Filled 8-Day Global 500 m), which is acquired via the Google Earth Engine platform. Compared to other products, the MOD16A2GF dataset offers advantages in spatial resolution (500 m) and temporal continuity (8-day intervals), enabling effective coverage and characterization of evapotranspiration changes across most of the windbreak and sand-fixation belt in this study area.

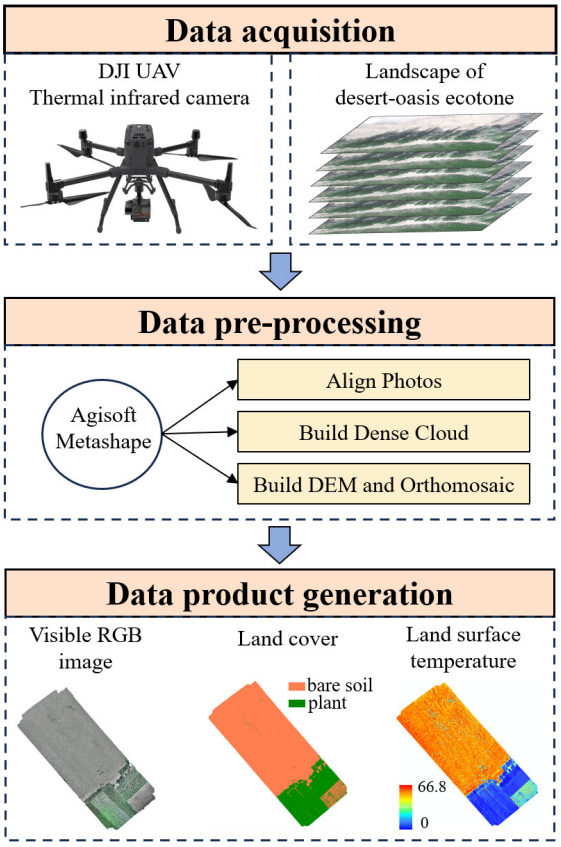


Figure 2. The processing flow of UAV thermal infrared remote sensing data.

2.3. Principles and Implementation of the Three-Temperature Model

The 3T model, proposed by Qiu et al. [26,32], estimates soil evaporation and vegetation transpiration by avoiding the complexity of aerodynamic resistance calculations. It uses only three key temperatures: actual surface temperature, reference surface (dry soil or non-transpiring leaf) temperature, and air temperature. The model performs separate calculations for bare soil and fully vegetated surfaces and combines the results for mixed pixels based on vegetation coverage [27].

2.3.1. Estimation of Soil Evaporation

The 3T model is based on the surface energy balance equation:

$$LE_G = R_{nG} - G - H_G \quad (1)$$

where LE_G is the latent heat flux of soil evaporation (W m^{-2}), and L is latent heat of vaporization (2.45 × 10^6 W m^{-2} mm^{-1}). R_{nG} is the net radiation at the soil surface (W m^{-2}) and G is the soil heat flux (W m^{-2}). H_G is the sensible heat flux from the soil surface that can be calculated by the following equation:

$$H_G = \frac{\rho C_\rho (T_G - T_\alpha)}{r_{aG}} \quad (2)$$

where ρ is air density (kg m^{-3}), C_ρ is the specific heat at constant pressure (MJ kg^{-1} °C^{-1}), T_G is the soil surface temperature (°C), T_α is the air temperature (°C), and r_{aG} is the aerodynamic resistance above the soil surface (s m^{-1}).

Qiu et al. [26] introduced a dry reference soil surface for which soil evaporation is assumed to be zero (LE_G = 0). Because the reference soil is assumed not to significantly

alter the surrounding atmospheric conditions, the aerodynamic resistance above the dry reference soil is considered equal to that above the actual soil surface. Therefore, r_{aG} can be expressed as:

$$r_{aG} = \frac{\rho C_\rho (T_{Gd} - T_\alpha)}{R_{nGd} - G_d} \quad (3)$$

where T_{Gd} is the temperature of the dry reference soil surface (°C), R_{nGd} is the net radiation of the dry reference soil surface (W m^{-2}), and G_d is the soil heat flux of the dry reference soil surface (W m^{-2}).

By combining Equations (1)–(3), soil evaporation can be estimated as:

$$LE_G = R_{nG} - G - (R_{nGd} - G_d)\frac{T_G - T_a}{T_{Gd} - T_\alpha} \quad (4)$$

2.3.2. Estimation of Vegetation Transpiration

For a fully vegetated surface, soil heat flux is assumed negligible. The canopy energy balance can therefore be written as:

$$LT_V = R_{nV} - H_V \quad (5)$$

where LT_V is the latent heat flux associated with vegetation transpiration (W m^{-2}), R_{nV} is the net radiation at the vegetation canopy surface (W m^{-2}), and H_V is the sensible heat flux from the canopy surface (W m^{-2}), which is calculated as:

$$H_V = \frac{\rho C_\rho (T_V - T_\alpha)}{r_{aV}} \quad (6)$$

where T_V is the canopy temperature (°C), T_α is the air temperature (°C), and r_{aV} is the aerodynamic resistance above the canopy (s m^{-1}).

Following the same approach used for soil evaporation, a non-transpiring reference leaf is introduced (LE_V = 0). Assuming that the atmospheric conditions surrounding the reference leaf do not differ significantly from those around the observed canopy, the aerodynamic resistance is considered identical. Thus:

$$r_{aV} = \frac{\rho C_\rho (T_{Vd} - T_\alpha)}{R_{nVd}} \quad (7)$$

where T_{Vd} is the temperature of the non-transpiring reference leaf (°C), and R_{nVd} is the net radiation of the reference leaf (W m^{-2}).

By combining Equations (5)–(7), the vegetation transpiration is expressed as:

$$LT_V = R_{nV} - R_{nVd}\frac{T_V - T_a}{T_{Vd} - T_\alpha} \quad (8)$$

2.3.3. Model Parameter Acquisition

(1) Reference surface temperature

The reference soil temperature (T_{Gd}) and reference canopy temperature (T_{Vd}) required by the 3T model were derived directly from UAV observations. First, high-resolution UAV imagery was classified into bare soil and vegetation using a supervised classification approach. The resulting land-cover map was then overlaid with the thermal infrared LST data. For each UAV transect, T_{Gd} and T_{Vd} were defined as the temperatures of the hottest bare-soil pixel and hottest vegetation pixel, respectively. Following the assumptions of the 3T model, these hottest pixels were considered to represent extremely water-limited conditions, under which evaporation or transpiration is negligible [27].

(2) Net radiation and soil heat flux

Net radiation is computed as:

$$\begin{aligned} R_n &= R_{swd} - R_{swu} + R_{lwd} - R_{lwu} \\ &= (1-\alpha)R_{swd} + \varepsilon_0\varepsilon_a\sigma T_a^4 - \varepsilon_0\sigma T_s^4 \end{aligned} \quad (9)$$

where R_{swd}, R_{swu}, R_{lwd}, and R_{lwu} are the incoming short-wave radiation, outgoing short-wave radiation, incoming long-wave radiation, and outgoing long-wave radiation, respectively. α is the land surface albedo, which is calculated through different bands of Landsat 8/9 images [33]. ε_0 is the land surface emissivity which can be calculated from NDVI [34]. ε_a is the atmospheric emissivity which can be estimated from air temperature [35]. σ is the Stefan–Boltzmann constant (5.67×10^{-8} W m^{-2} K^{-4}). T_α is air temperature (K), and T_s is land surface temperature (K).

Soil heat flux was assumed negligible under complete vegetation cover (G = 0). Otherwise, soil heat flux was estimated as a fraction of net radiation [36]:

$$G = R_n[\gamma_c + (1-f)(\gamma_s - \gamma_c)] \quad (10)$$

where f is the fractional vegetation cover, derived from supervised classification of the high-resolution UAV orthomosaic into vegetation and bare-soil classes and calculated as the proportion of vegetation area within each analysis pixel. γ_s and γ_c are empirical coefficients, where γ_s = 0.315 [37] and γ_c = 0.05 [38].

The reference net radiation was calculated using the same procedure as Equation (9). For the dry reference canopy, albedo, land emissivity, and land surface temperature, values of 0.225, 0.990, and T_{Vd} were assigned, respectively. For the dry reference soil, corresponding values of 0.275, 0.970, and T_{Gd} were used. Following the original 3T model parameterization, the reference soil heat flux was estimated as 31.5% of its reference net radiation [27].

(3) Meteorological data

Because the study area is located in a remote desert-oasis ecotone and no site-based meteorological observations were available during the UAV survey period, meteorological forcing data were obtained from the fifth-generation ECMWF Land Reanalysis dataset (ERA5-Land). Variables including air temperature, wind speed, atmospheric pressure, relative humidity, and soil temperature were used as meteorological inputs for all model calculations.

2.4. Scaling UAV-Derived Instantaneous ET to Daily Value

The UAV-derived ET represents instantaneous fluxes, which were scaled to daily values following Jackson et al. [39], based on the assumption of a sinusoidal diurnal variation in solar radiation under clear-sky daytime conditions:

$$ET_d = ET_i \frac{2N}{\pi \sin(\pi t / N)} \quad (11)$$

where ET_d and ET_i are the daily and instantaneous ET, respectively. N is the duration of sunshine, and t is the elapsed time from sunrise to the UAV observation time.

2.5. Model Validation Methods

To comprehensively assess the accuracy of the 3T model simulations, two independent validation strategies were employed. Spatial-scale validation (area-based): Due to the lack of field ET measurements in the study area, the SEBAL model was adopted as a reference

model for spatial comparison to assess the consistency of ET spatial patterns across different land-cover types [40]. Using the same input data (LST, meteorology, and albedo), the SEBAL model was executed, and its ET outputs were compared pixel-by-pixel with those from the 3T model. Evaluation metrics included the coefficient of determination (R^2) and root mean square error (RMSE). Point-scale validation: A two-source model based on soil–vegetation–atmosphere transfer processes was used for validation [41]. This model independently estimates transpiration and evaporation at the patch scale. The mean ET values simulated by the two-source model for the 14 transects were compared with the statistical means (and spatial variation ranges) derived from the 3T model for the corresponding transects, and the absolute errors were calculated. Detailed equations and parameterizations of the SEBAL and two-source models are provided in Appendix A.

2.6. Temperature Gradient Based Vegetation Water Stress Index

To better interpret the spatial variability of ET estimated by the 3T model, TVDI and TCI were calculated as auxiliary indicators of surface moisture status and vegetation thermal stress. These indices were used to analyze the relationships between ET patterns, drought conditions, and vegetation responses across the desert-oasis ecotone.

The temperature vegetation dryness index (TVDI) was employed to characterize relative surface moisture conditions. By combining UAV-derived land surface temperature (LST) with the normalized difference vegetation index (NDVI) derived from Landsat imagery, an LST–NDVI feature space was constructed to determine the dry and wet edges and calculate TVDI values [42]. The integration of high-resolution UAV thermal data with Landsat NDVI information enables a detailed assessment of spatial variations in surface moisture across the desert-oasis ecotone.

The Temperature Condition Index (TCI) was used to characterize vegetation thermal stress based on LST [25]. Unlike TVDI, TCI relies solely on thermal information and therefore reflects vegetation temperature responses associated with transpiration and physiological regulation. Owing to the sub-meter spatial resolution of the UAV thermal imagery, TCI can effectively capture fine-scale temperature differences among vegetation types and provide additional insights into the relationship between vegetation stress and ET patterns. The TCI was calculated as:

$$TCI = 1 - \frac{T_{max} - T}{T_{max} - T_{min}} \quad (12)$$

where $T_{\max}$ and $T_{\min}$ represent the maximum and minimum pixel temperatures (°C) within each UAV transect, respectively. T denotes the temperature of each individual pixel (°C). Calculated TCI values were constrained to the range of 0–1.

3. Results

3.1. Model Validation Results

Comparison with the SEBAL model: The spatial patterns of ET simulated by the 3T and SEBAL models were highly consistent (Figure 3). Given the heterogeneous terrain conditions across all UAV transects, a stratified pixel-wise comparison was further conducted based on land-cover types (cropland, shelterbelt, desert vegetation, and bare soil). The results showed strong agreement between the two models, with R^2 ranging from 0.90 to 0.95 and RMSE from 0.22 to 0.43 mm d^{-1} across different land-cover types. These results indicate that the 3T model reliably reproduces the spatial variability of ET across heterogeneous desert-oasis landscapes.

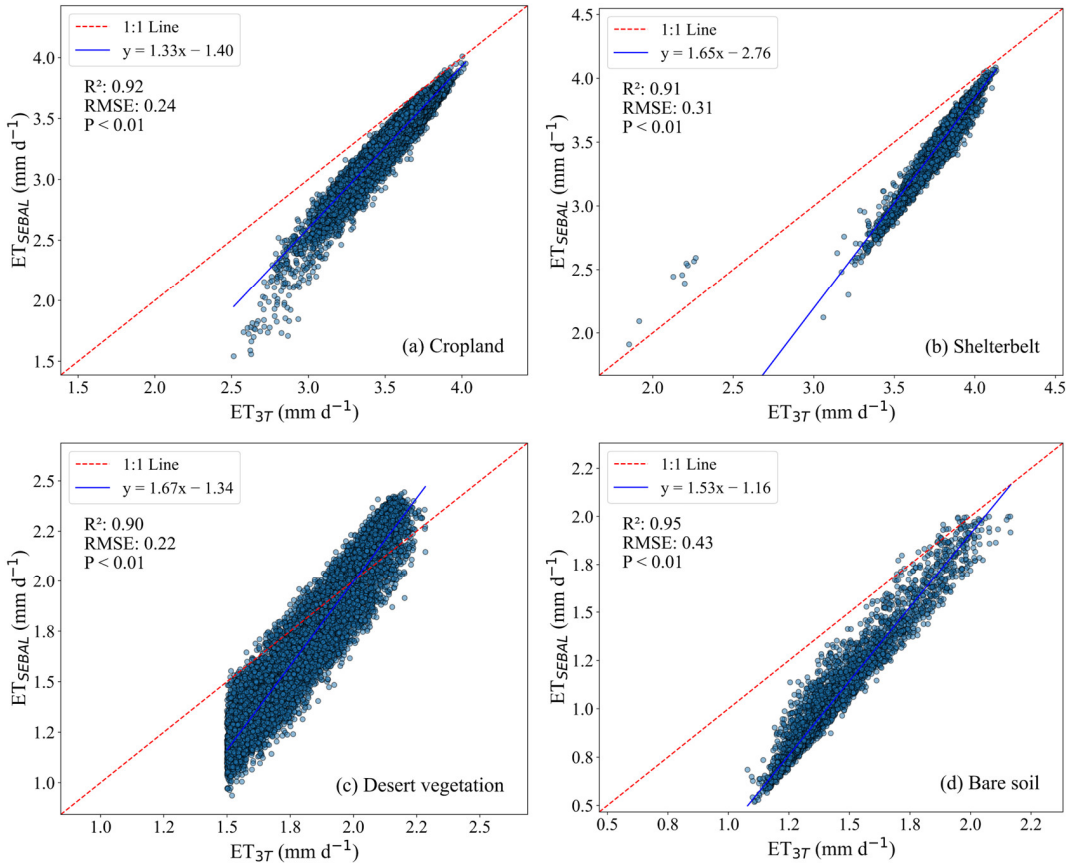


Figure 3. Statistical comparison of ET simulated by the 3T model and SEBAL model across different land-cover types.

Comparison with the two-source model: The mean ET values simulated by the two-source model for each transect all fell within the range of ET values estimated by the 3T model for the corresponding transect (Figure 4 and Table 2). The mean absolute error was 0.38 mm d^{-1} and the RMSE was 0.45 mm d^{-1}. Notably, larger deviations were observed at HX9, HX10, and HX14, which are associated with highly heterogeneous land-cover composition and topographic shading effects of sand dunes. Overall, the results indicate good agreement between the two models at the transect-average scale.

Table 2. Statistical comparison of simulation results between the 3T model and the two-source model [1].

Site	Three-Temperature Model			Two-Source Model	Absolute Error
	Minimum	Maximum	Mean		
HX1	0.00	4.79	1.92	2.09	0.17
HX3	0.33	7.59	2.83	3.34	0.51
HX4	0.00	9.21	3.16	2.63	0.53
HX5	0.05	8.80	3.21	2.94	0.27
HX6	0.27	6.98	2.07	1.62	0.45
HX7	0.12	7.01	2.54	2.08	0.46
HX8	0.00	7.89	3.36	3.19	0.17
HX9	0.06	7.48	2.77	2.12	0.65
HX10	0.09	8.32	2.46	1.71	0.75

Table 2. *Cont.*

Site	Three-Temperature Model			Two-Source Model	Absolute Error
	Minimum	Maximum	Mean		
HX11	0.09	8.00	2.97	3.00	0.03
HX12	0.28	6.46	2.47	2.41	0.06
HX13	0.64	8.93	3.31	3.06	0.25
HX14	0.19	9.56	2.35	1.57	0.78
HX15	0.08	10.69	3.67	3.90	0.23

[1] All values are in mm d^{-1}.

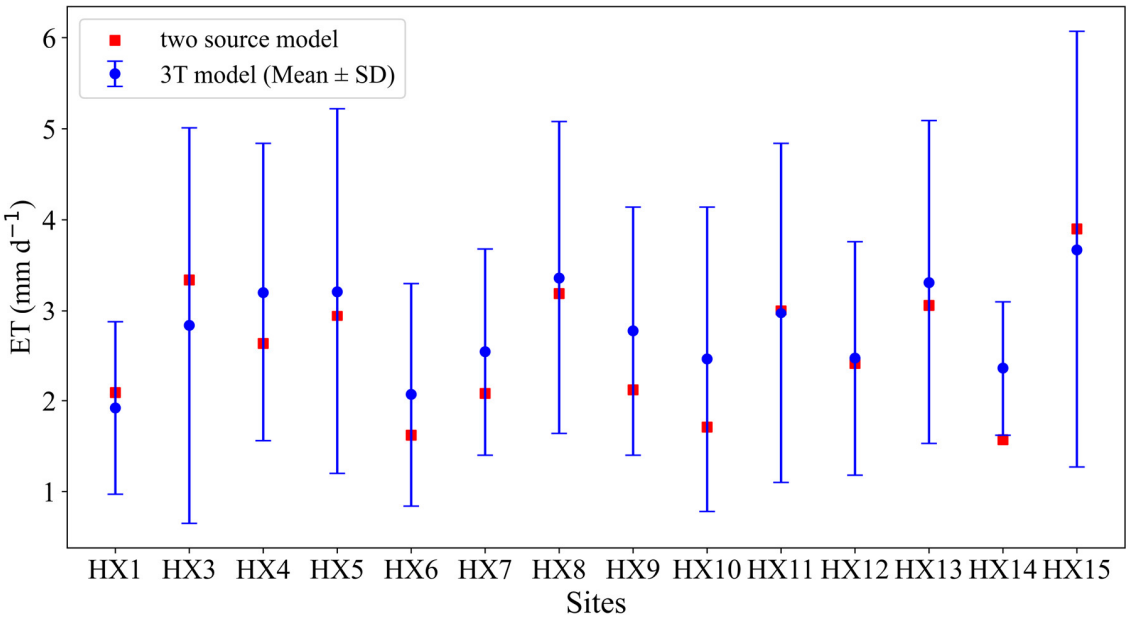


Figure 4. Comparison of mean ET and its spatial variability estimated by the 3T model and the two-source model.

3.2. Spatiotemporal Dynamics of Evapotranspiration in the Desert-Oasis Ecotone

The ET spatial distribution maps generated by the UAV-3T method (Figure 5) clearly reveal the strong spatial heterogeneity of the desert-oasis ecotone. ET values exhibited a pronounced decreasing gradient from oasis cropland towards the desert interior. Cropland areas, supported by irrigation and characterized by high crop transpiration, showed the highest ET values, locally reaching 3–10.69 mm d^{-1}. Shelterbelt zones had intermediate ET values, mostly between 3 and 6 mm d^{-1}, with patchy variations due to differences in tree species and density. Desert areas with sparse vegetation and water limitation showed the lowest ET, generally below 3 mm d^{-1}, with mobile sand dunes dominated by soil evaporation having the minimum values. The spatial distribution of ET correlated highly with land-cover type, vegetation characteristics, and soil moisture conditions.

The daily equivalent transpiration was extracted from thermal infrared-based ET maps with vegetation types identified using visible-band imagery. These values represent scaled daily estimates derived from instantaneous UAV observations using a sinusoidal temporal upscaling approach (see Materials and Methods Section 2.4). The results show clear differences in water consumption among vegetation types in the desert-oasis ecotone. Cropland exhibited the highest transpiration rates (mean 5.92 mm d^{-1}), followed by shelterbelt vegetation (mean 5.23 mm d^{-1}), while desert vegetation showed the lowest values (mean 3.12 mm d^{-1}) (Figure 6a). Transpiration variability was greatest among tree species within shelterbelts, indicating pronounced differences in water-use strategies,

whereas desert vegetation displayed consistently low transpiration with relatively small variability, reflecting conservative and stable water-use characteristics.

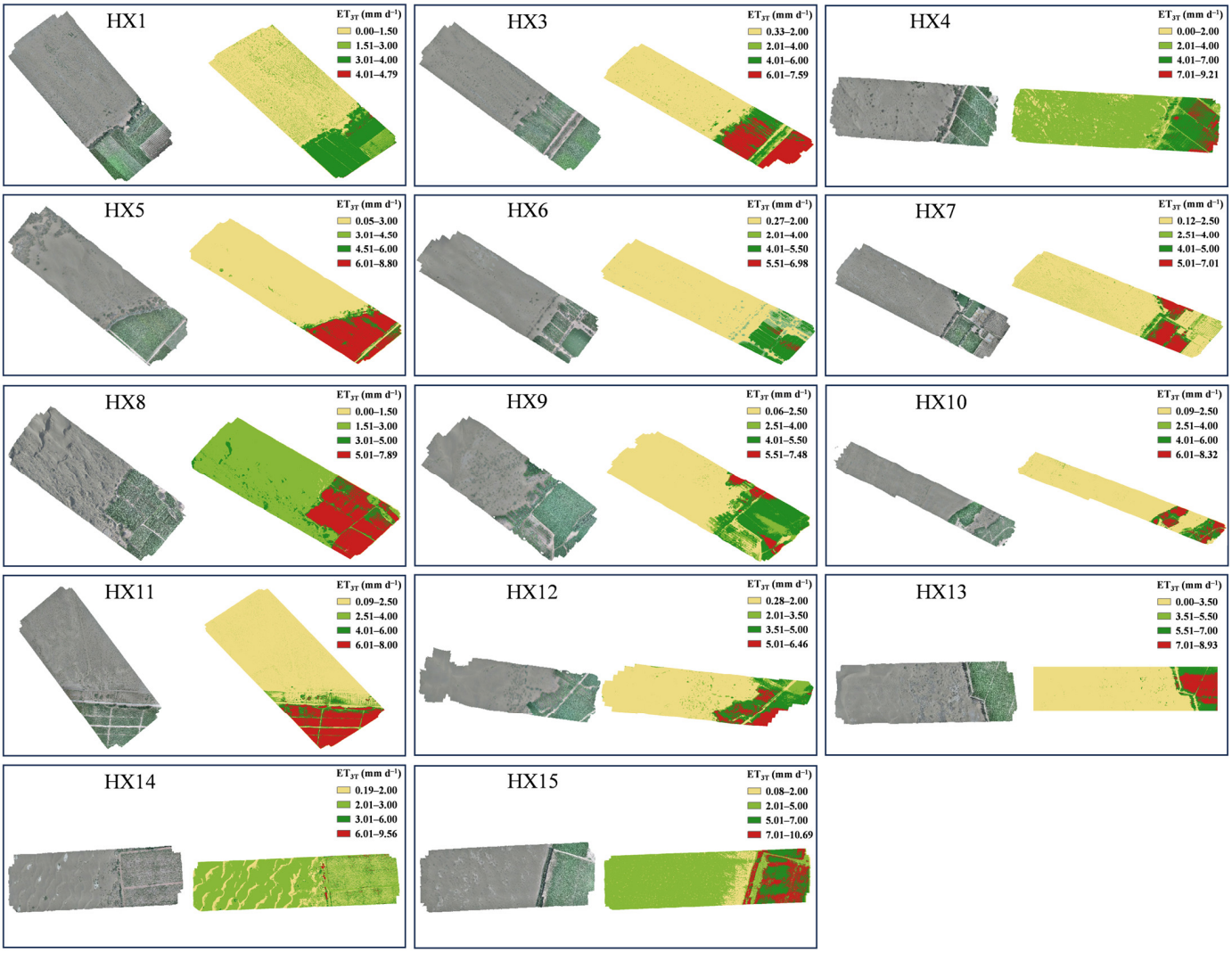


Figure 5. Spatial distribution pattern of ET in the desert-oasis ecotone of the Hexi Corridor. Each subplot corresponds to one UAV transect (HX1–HX15). In each panel, the left image shows the RGB orthomosaic and the right image shows the corresponding ET map derived from the 3T model. Due to the pronounced spatial heterogeneity of ET across land-cover types (cropland, shelterbelts, desert vegetation and bare soil) in the desert-oasis ecotone, ET values are classified into discrete intervals for visualization. The color legend represents ET ranges (mm d^{-1}), with warmer colors indicating higher ET intensity.

At the species level, maize exhibited higher transpiration than alfalfa in cropland. Within shelterbelts, elm and poplar showed relatively high transpiration, while Russian olive had lower values. Among sand-stabilizing vegetation, common reed and tamarisk exhibited relatively high transpiration, whereas xerophytic shrubs such as saxaul, red sand shrub and nitraria showed much lower transpiration rates. Overall, differences in vegetation transpiration are primarily controlled by vegetation type, species composition, and associated water acquisition and use strategies (Figure 6b).

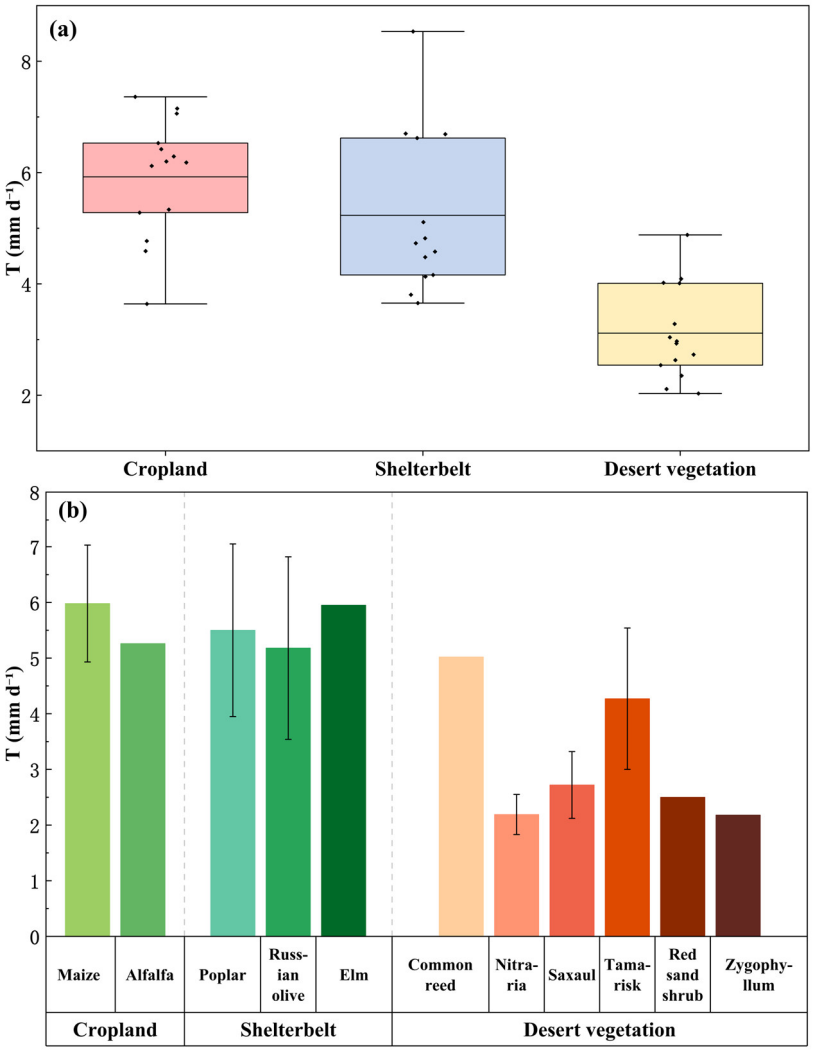


Figure 6. Transpiration characteristics of representative vegetation types in the desert-oasis ecotone. The analysis is conducted over the entire desert-oasis ecotones (HX1–HX15), with results further stratified by land-cover type and vegetation category. (**a**) Boxplots of daily transpiration rates for cropland, shelterbelt, and desert vegetation. Boxes represent the interquartile range (25th–75th percentiles), central lines indicate medians, and whiskers extend to 1.5 × IQR. Black dots represent individual observations. (**b**) Mean daily transpiration rates of individual vegetation types. Error bars represent the standard deviation. All values are expressed in mm d^{-1}.

Based on ET time series derived from remote sensing evapotranspiration products for the period from 1 January 2022 to 18 December 2024, ET in the desert-oasis ecotone exhibited pronounced seasonal and interannual variability, characterized primarily by unimodal or bimodal temporal patterns (Figure 7). Most sites (HX1, HX3, HX4, HX9, HX10, and HX12) showed a clear unimodal seasonal cycle, with low ET during the non-growing season (January–May), generally below 1 mm d^{-1}, and substantially higher ET during the growing season (June–October), typically ranging from 2 to 3 mm d^{-1}. Among these sites, HX1 exhibited markedly higher growing season ET than the others, with peak values reaching approximately 6 mm d^{-1}. In contrast, HX5, HX6, HX7, and HX8 displayed bimodal patterns, with relatively elevated ET in both winter and summer; however, their overall daily ET remained low throughout the year, fluctuating around 1 mm d^{-1}.

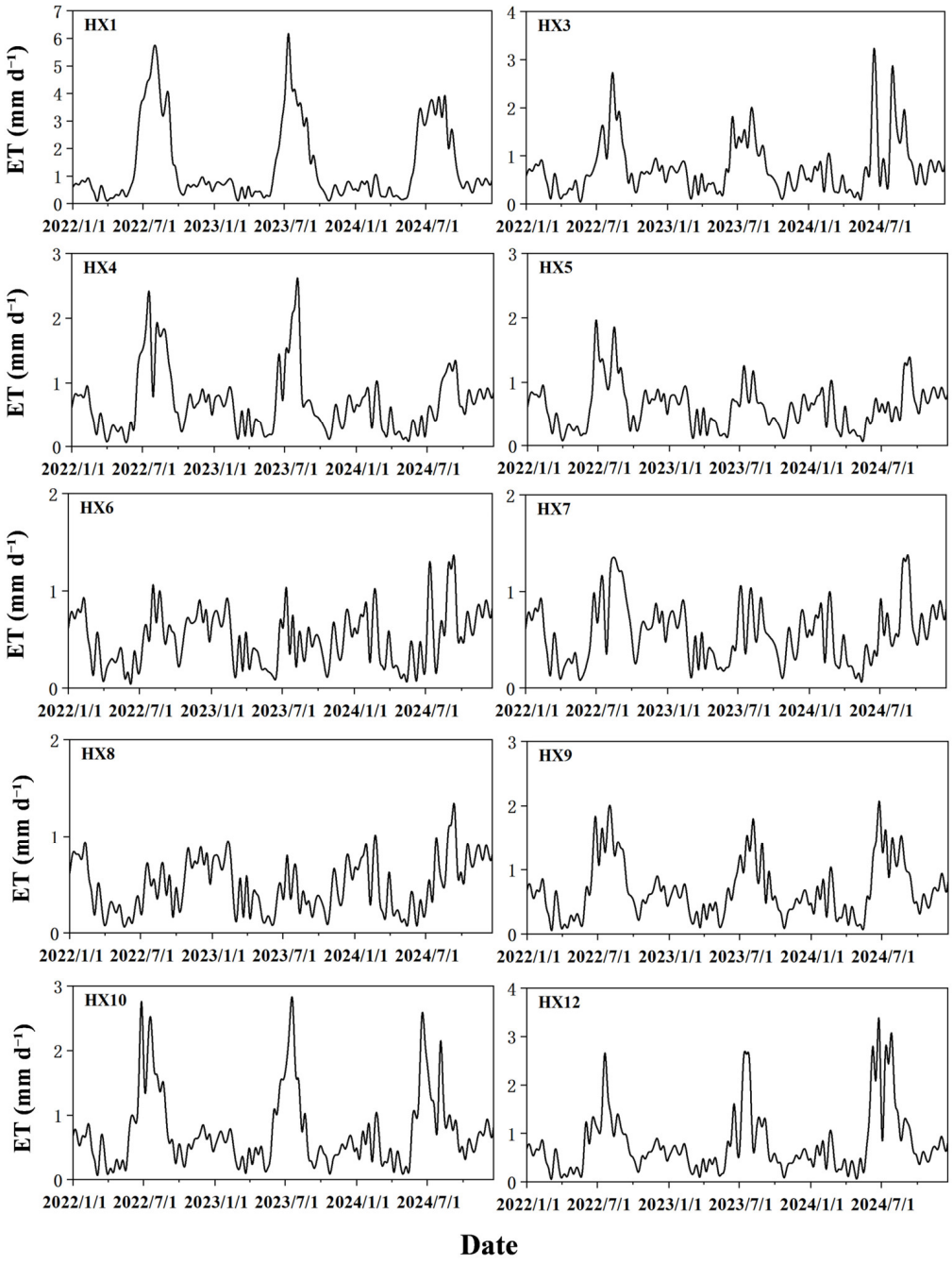


Figure 7. Diurnal variation in evapotranspiration in the desert-oasis ecotone during 2022–2024.

3.3. Water Stress Across Different Land-Cover Types of the Desert-Oasis Ecotone

To better interpret the spatial variability of ET (Figure 5), the TVDI results (Figure 8) were analyzed jointly with ET patterns. Areas with higher TVDI values generally corresponded to lower ET, while lower TVDI values were associated with higher ET, indicating a strong coupling between surface dryness conditions and evapotranspiration. Vegetated areas exhibited consistently lower TVDI values than bare soil, reflecting enhanced moisture availability and vegetation regulation of surface water loss.

To investigate drought responses among different vegetation types in the desert-oasis ecotones, temperature condition index (TCI) values were analyzed for 11 representative plant species across 14 study sites, with higher TCI values indicating stronger drought stress. The results show significant interspecific differences in TCI (Figure 9). Russian olive, tamarisk, and poplar exhibited relatively high TCI values at multiple sites, indicating

stronger drought stress, with Russian olive at HX5 showing the highest TCI value (0.73). In contrast, maize and saxaul displayed lower TCI values at some sites (e.g., HX1 and HX15), suggesting weaker drought stress, while nitraria and alfalfa consistently exhibited moderate TCI levels across all sites. These results indicate substantial differences in drought response and adaptation among plant species within the sand-fixing shelterbelt.

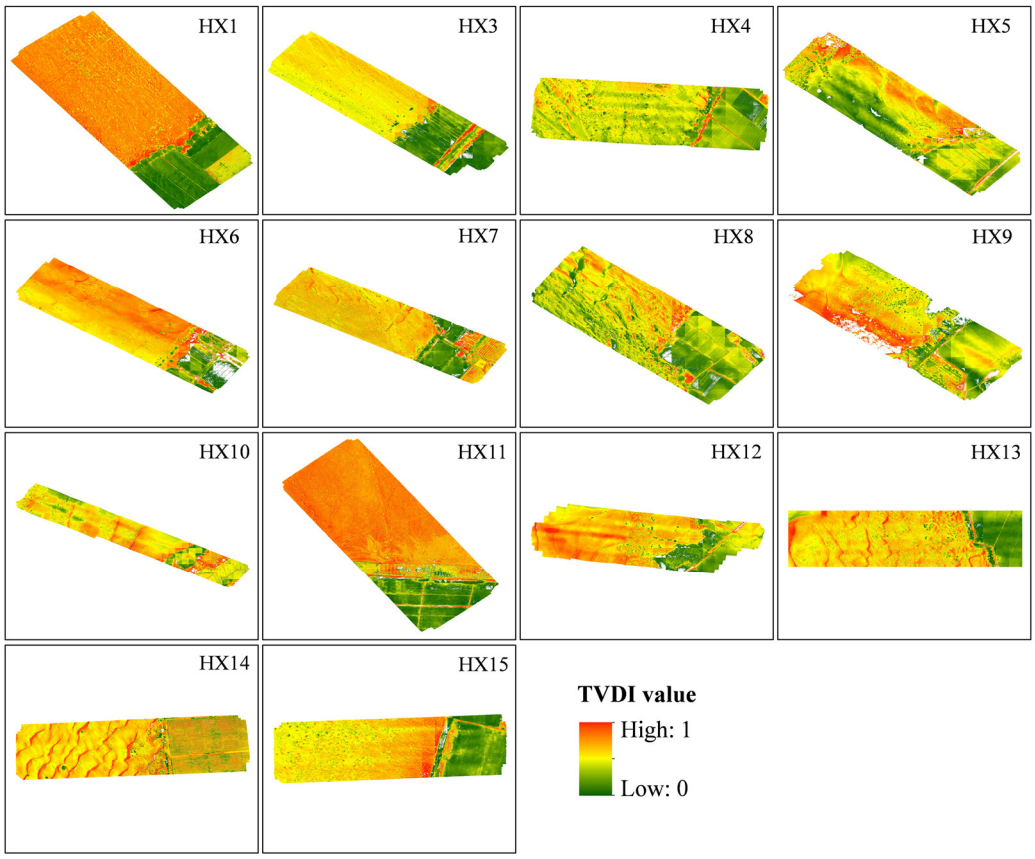


Figure 8. Spatial distribution of the temperature vegetation dryness index (TVDI) in the desert-oasis ecotone. Each subplot corresponds to one UAV transect (HX1–HX15). The index is displayed as a continuous variable ranging from 0 to 1, where higher values indicate stronger surface dryness conditions and lower values indicate wetter conditions. The color bar represents TVDI values (dimensionless).

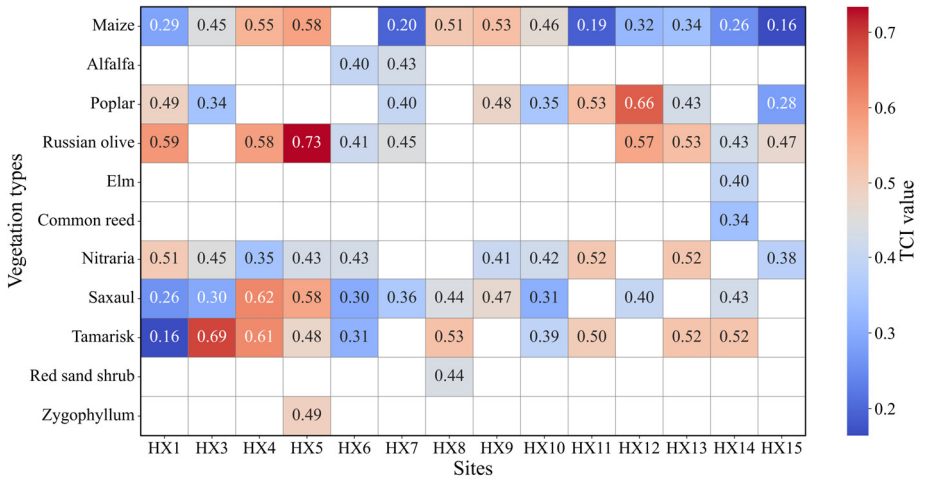


Figure 9. Temperature condition index (TCI) characteristics of representative vegetation types in the desert-oasis ecotone.

4. Discussion

4.1. Applicability and Advancement of the 3T Model in Desert-Oasis Ecotones

This study demonstrates that coupling the 3T model with high-resolution UAV thermal infrared imagery provides an effective approach for estimating ET in desert-oasis ecotones. The main contributions of this work are threefold: (1) integrating sub-meter UAV thermal observations into the 3T framework to resolve fine-scale ET heterogeneity; (2) establishing a practical workflow applicable to data-scarce and ungauged desert regions; and (3) validating the model using both the SEBAL model and a two-source energy balance model.

The high spatial resolution provided by UAV thermal imagery substantially improves the representation of heterogeneous surface features compared with conventional satellite-based approaches. Fine-scale landscape elements, such as linear shelterbelts, isolated shrub patches, and fragmented bare-soil areas, can be explicitly resolved (Figure 10), enabling more accurate characterization of spatial variations in ET. In addition, the simplified aerodynamic parameterization of the 3T model makes it particularly suitable for arid regions where meteorological observations are limited. By combining detailed field surveys, synchronous environmental measurements and high-resolution UAV observations, this study provides essential local parameters that enhance the applicability of the model in ungauged areas. Furthermore, the use of two independent validation approaches, including pixel-scale comparison with the SEBAL model and transect-scale comparison with the two-source model, increases confidence in the robustness of the proposed framework across different land-cover types.

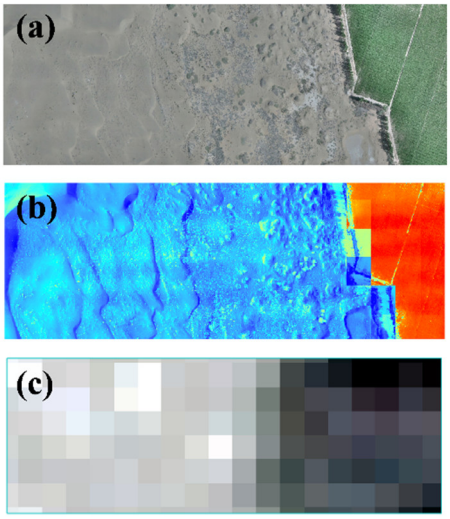


Figure 10. Fine-scale comparison of spatial information representation in the desert-oasis ecotone. (**a**) UAV visible-light image. (**b**) High-resolution ET map derived from UAV thermal infrared imagery (spatial resolution <1 m). (**c**) Coarse-resolution ET map derived from Landsat imagery (spatial resolution 30 m). This comparison highlights the differences in spatial detail representation between UAV and satellite observations.

Despite these advantages, several limitations should be acknowledged. First, the reference dry temperatures required by the 3T model were determined using the highest observed surface temperatures in each UAV survey, which may be influenced by image noise and local surface heterogeneity. Second, meteorological forcing data were obtained from the ERA5-Land reanalysis dataset because no synchronous field observations were available during the UAV campaigns. Although ERA5-Land provides spatially consistent atmospheric forcing for remote desert regions, it cannot fully capture local microclimatic variability. Third, owing to the absence of direct ET observations, model evaluation relied

on comparisons with two independently established ET models rather than absolute validation against eddy-covariance or lysimeter measurements. Future studies incorporating continuous field observations will further improve the assessment of model accuracy and broaden its applicability.

4.2. Sources of Uncertainty

The uncertainties in this study primarily originate from model parameterization and remote sensing data processing, among which the determination of reference dry temperature represents the most influential source of uncertainty for the 3T model. In this study, reference dry temperatures were defined using the highest observed surface temperatures from each UAV flight. Although this approach is commonly adopted in thermal-based evapotranspiration models, it remains sensitive to image noise, sub-pixel heterogeneity, and mixed land-cover conditions, particularly in highly fragmented desert-oasis ecotones [26,32]. To improve the robustness of reference temperature estimation, future studies should consider physically based calibration approaches, such as the simultaneous deployment of dry sand trays and in situ measurements of non-transpiring vegetation under controlled water stress conditions, to better define theoretical dry boundaries.

The second major source of uncertainty arises from the derivation of fractional vegetation cover (FVC) from high-resolution UAV imagery. Although supervised classification enables detailed representation of surface heterogeneity, shadow-affected pixels in UAV orthomosaics may introduce systematic misclassification, whereby shaded soil surfaces are incorrectly identified as vegetation. Such misclassification can propagate into errors in the partitioning of evapotranspiration components, potentially biasing the separation between soil evaporation and plant transpiration [43,44]. This highlights the importance of improving shadow correction or incorporating multi-angle or radiometrically corrected imagery in future studies.

Uncertainty also arises in the estimation of net radiation under heterogeneous surface and terrain conditions. Complex land surface composition and topographic variability may introduce biases in radiative flux calculations [45]. Incorporating higher-resolution meteorological forcing and terrain-corrected radiation schemes may help reduce these uncertainties. Furthermore, the model exhibited overestimation trends in extremely arid bare-soil areas, likely due to insufficient representation of the nonlinear response of soil surface resistance under dry conditions [46]. Future implementations could integrate dynamic soil–air resistance parameterizations or couple soil moisture constraints to enhance the mechanistic representation of evapotranspiration in drylands.

Overall, these uncertainties emphasize the importance of improving ground-based calibration and multi-source observational constraints in high-resolution UAV-based evapotranspiration modeling.

4.3. Limitations

Despite the encouraging results, several limitations should be acknowledged. First, this study was based on a single UAV campaign conducted during the growing season, which limits the evaluation of seasonal and interannual variations in evapotranspiration dynamics. Second, owing to the absence of eddy covariance or lysimeter measurements in the desert-oasis ecotone, model performance was assessed using two independently established ET models rather than direct ground observations. Although this multi-model validation provides relative confidence in the spatial patterns simulated by the 3T model, future studies incorporating continuous field measurements will enable a more rigorous assessment of absolute model accuracy. Finally, the proposed framework has been evaluated

only in desert-oasis ecotones, and its applicability to other dryland ecosystems requires further investigation.

4.4. Implications and Vegetation Optimization Design for the Windbreak and Sand-Fixation in the Hexi Corridor

The spatial and seasonal patterns of ET revealed here underscore the strong control of water availability and vegetation type on ecohydrological processes, with a declining ET gradient from cropland to desert, highlighting the trade-off between agricultural water use and natural vegetation sustainability. Notably, the negative correlation between LAI and ET observed in shelterbelts may reflect potential over-planting effects and the resulting eco-physiological trade-offs. Under high planting density, competition for limited soil moisture is likely intensified, increasing the risk of water stress. Plants subjected to prolonged water stress typically reduce stomatal conductance by closing their stomata to limit water loss, thereby suppressing transpiration despite a higher leaf area index [47–49]. This coupled structural–physiological mechanism provides a plausible explanation for the reduced ET observed at higher LAI levels and highlights the importance of balancing planting density with regional water-carrying capacity rather than simply maximizing vegetation cover.

From a vegetation management perspective, these results imply that sand-fixation system design should consider regional water availability rather than simply maximizing vegetation cover. In water-scarce regions like Minqin, reducing planting density and selecting deep-rooted, low-water-use species (e.g., *Nitraria*, *Haloxylon*) can alleviate water stress while maintaining sand stabilization, whereas in relatively water-sufficient areas like Linze, strategic increases in cover, using species such as *Tamarix* and *Phragmites*, can enhance ecological barriers without exceeding hydrological limits [50–52]. This study also highlights the importance of species-specific water-use strategies, as plants with dimorphic root systems (e.g., *Haloxylon*, *Reaumuria*) show greater flexibility in accessing shallow and deep water sources, making them resilient to rainfall variability, in contrast to species reliant on single water sources (e.g., *Zygophyllum*) that may be more vulnerable to drought—integrating such functional traits into planting schemes can improve community resilience and water-use efficiency [53–55]. In summary, this research advances the application of UAV-based thermal remote sensing in arid zone ecohydrology and provides a validated, scalable framework for vegetation optimization in sand-fixation belts, with future work recommended to incorporate multi-temporal UAV campaigns and integrate groundwater and irrigation inputs to refine ET estimates and vegetation-carrying capacity models under realistic water management scenarios.

5. Conclusions

This study developed a high-resolution ET mapping framework for the Hexi Corridor desert-oasis ecotone by integrating UAV-based thermal infrared remote sensing with the 3T model. The proposed approach enables detailed characterization of spatial ET patterns across heterogeneous landscapes. The performance of the model was evaluated against both the SEBAL model and a two-source energy balance model, showing overall good agreement and reliable representation of spatial variability. Future research should focus on improving the representation of dryland surface conditions through more robust parameterization of reference temperature and net radiation. In addition, extending UAV observations to multi-temporal acquisitions is essential for capturing seasonal dynamics of ET. A further important direction is the development of spatiotemporal fusion frameworks that integrate UAV thermal observations with medium-resolution satellite data (e.g., Landsat or Sentinel-2), enabling the simultaneous achievement of high spatial resolution and long-term continuous monitoring of ET dynamics.

Author Contributions: S.L.: Investigation, Data curation, Software, Visualization, Writing—Original draft preparation. Reviewing and Editing. P.W.: Conceptualization, Methodology, Supervision, Funding acquisition; Writing—Reviewing and Editing. Y.X.: Investigation, Resources, Writing—Review and Editing. D.Z.: Resources, Supervision, Writing—Review and Editing. All authors have read and agreed to the published version of the manuscript.

Funding: The study was financially supported by Major Science and Technology Program of Inner Mongolia Autonomous Region (2024JBGS0013-03) and Joint Fund Project of the National Natural Science Foundation of China (U21A2001).

Data Availability Statement: Data will be made available on request.

Conflicts of Interest: The authors declare no conflicts of interest.

Appendix A

Appendix A.1. SEBAL Model

The inversion results of evapotranspiration from the Three-Temperature Model were validated through pixel-by-pixel comparison with those from the Surface Energy Balance Algorithm for Land (SEBAL) model. The SEBAL model, proposed by Bastiaanssen et al. [40], is a regional evapotranspiration estimation model. Both the SEBAL model and the Three-Temperature Model are based on the surface energy balance principle (Equations (1) and (5)) and share consistency in core input parameters, including net radiation, surface temperature, and air temperature. The main distinction between the two lies in their approaches to calculating sensible heat flux: the Three-Temperature Model simplifies the computation of sensible heat flux by introducing a reference surface, whereas the SEBAL model requires solving for sensible heat flux directly as a critical step.

The sensible heat flux for soil and vegetation surfaces is calculated using the following equations:

$$H_G = \frac{\rho C_\rho (T_G - T_\alpha)}{r_{aG}} \tag{A1}$$

$$H_V = \frac{\rho C_\rho \ (T_V - T_a)}{r_{aV}} \tag{A2}$$

r_{aG} and r_{aV} are the aerodynamic resistances above the soil and vegetation surfaces (s m^{-1}), respectively, and can be calculated using the following formulas:

$$r_{aG} = ln\left(\frac{z_m}{z_{0mG}}\right) ln\left(\frac{z_h}{z_{0hG}}\right) / k^2 u \tag{A3}$$

$$r_{aV} = ln\left(\frac{z_m - d_0}{z_{0mV}}\right) ln\left(\frac{z_{h-d_0}}{z_{0hV}}\right) / k^2 u \tag{A4}$$

where z_m is the measurement height of wind speed (m), z_h is the measurement height of temperature and humidity (m), z_{0mG} is the roughness length governing momentum transfer over soil (=10^{-4}, m), z_{0hG} is the roughness length governing heat transfer over soil (=$0.1 z_{0mG}$, m), d_0 is the zero-plane displacement height (=$0.666 z_v$, where z_v is vegetation height, m), z_{0mv} is the roughness length governing momentum transfer above the vegetation canopy (=$0.123 z_v$, m), z_{0hv} is the roughness length governing heat transfer above the vegetation canopy (=$0.1 z_{0mv}$, m), k is the Kármán constant (=0.41), and u is the wind speed (m·s^{-1}).

The SEBAL model calculates soil heat flux using an empirical formula:

$$G_S = 0.2 \ R_{nG} \tag{A5}$$

$$G_V = \frac{T_V}{\rho}\left(0.0038\,\rho + 0.0074\rho^2\right)\left(1 - 0.98NDVI^4\right)R_{nV} \quad \text{(A6)}$$

where G_S and G_V represent the soil heat flux for bare soil and vegetated surfaces (W m^{-2}), respectively, and ρ is the surface albedo.

Appendix A.2. Two-Source Model with Numerical Solution

This study employs a two-source energy balance model to estimate evapotranspiration from windbreak and sand-fixing belts, and conducts localized comparative validation against simulation results from the Three-Temperature Model. The dual-source model, by establishing separate radiation/energy balance equations for vegetation patches and bare soil surfaces, achieves a disaggregation of evapotranspiration. Furthermore, this model incorporates the controlling effects of vegetation stomatal conductance and soil moisture on the evapotranspiration process from the bottom up [41,56].

The main governing equations and parameter settings of the model are as follows:

$$R_{nV} = (1 - f_V)\left[(1 - a_V)S_d + L_d + \sigma {T_G}^4 - 2\sigma {T_L}^4\right] = H_V + lT \quad \text{(A7)}$$

$$R_{nG} = f_V[(1 - a_G)S_d + L_d] + (1 - f_V)\sigma {T_L}^4 - \sigma {T_G}^4 = G + H_G + lE \quad \text{(A8)}$$

Among them, R_{nV} denotes the canopy net radiation of vegetation patches (W m^{-2}); H_V represents the canopy sensible heat flux of vegetation patches (W m^{-2}); T refers to the total vegetation transpiration rate (kg m^{-2} s^{-1}); f_V signifies the dielectric constant of vegetation canopies; S_d stands for the downward shortwave radiation (W m^{-2}); L_d denotes the downward longwave radiation (W m^{-2}); σ is the Stefan–Boltzmann constant (=5.67 × 10^{-8} W m^{-2} K^{-4}); T_G represents the surface temperature of desert-oasis ecotones (°C); T_L denotes the leaf temperature of desert-oasis ecotones (°C); R_{nG} refers to the surface net radiation flux (W m^{-2}); G stands for the soil heat flux (W m^{-2}); H_G represents the surface sensible heat flux (W m^{-2}); E refers to the soil evaporation rate (kg m^{-2} s^{-1}); α_G signifies the surface albedo; and α_V denotes the vegetation canopy albedo.

The soil heat flux G can be calculated using the following formula:

$$G = \lambda_{soil}(T_G - T_{soil})/z_{soil} \quad \text{(A9)}$$

where λ_{soil} is the thermal conductivity of the topsoil (W m^{-1} K^{-1}), T_{soil} is the soil temperature at a specific depth (°C), z_{soil} is the soil depth (m). In this study, λ_{soil} is assumed to be a constant (=1).

Vegetation transpiration (T) and soil evaporation (E) can be expressed as follows:

$$T = \rho_a[q_{sat}(T_L) - q_a]/(r_{aV} + r_c) \quad \text{(A10)}$$

$$E = \rho_a[q_{sat}(T_G) - q_a]/(r_{aG} + r_{ss}) \quad \text{(A11)}$$

where $q_{sat}(T_L)$ is the saturation-specific humidity corrected by leaf temperature (kg kg^{-1}), $q_{sat}(T_G)$ is the saturation-specific humidity corrected by soil temperature, q_a is the air-specific humidity, r_c is the vegetation canopy resistance (s m^{-1}), and r_{ss} is the soil surface resistance (s m^{-1}).

The formulas for calculating the resistance of vegetation and soil surface are given below:

$$r_c = r_{st}/LAI \quad \text{(A12)}$$

$$r_{ss} = a(\theta_{max}/\theta)^b + c \quad \text{(A13)}$$

where r_{st} denotes the leaf stomatal resistance and *LAI* is the leaf area index; a, b and c are empirical coefficients (a = 3.5, b = 2.3, c = 433.5); θ is the volumetric soil water content ($m^3\ m^{-3}$); θ_{sat} is the saturated volumetric soil water content ($m^3\ m^{-3}$).

$$r_{st} = \frac{r_{st_min}}{c_{sw}} + \frac{r_{st_max} - r_{st_min}}{c_{sw}} \left\{ 1 - \tanh\left(\frac{S_d}{c_{sd}} \right) \right\} \quad \text{(A14)}$$

where r_{st_min} and r_{st_max} represent the minimum and maximum values of leaf stomatal resistance under saturated soil moisture conditions, which are finally set as r_{st_min} = 100, r_{st_max} = 10,000, through the trial-and-error method; c_{sd} = 25 W m^{-2}.

$$c_{sw} = \frac{\theta}{\theta_{max}} \quad \text{(A15)}$$

References

1. Rosenberg, N.J.; Blad, B.L.; Verma, S.B. *Microclimate: The Biological Environment*; John Wiley & Sons: Hoboken, NJ, USA, 1983.
2. Jung, M.; Reichstein, M.; Ciais, P.; Seneviratne, S.I.; Sheffield, J.; Goulden, M.L.; Bonan, G.; Cescatti, A.; Chen, J.; De Jeu, R. Recent decline in the global land evapotranspiration trend due to limited moisture supply. *Nature* **2010**, *467*, 951–954. [CrossRef]
3. Zhao, W.; Liu, B.; Chang, X.; Yang, Q.; Yang, Y.; Liu, Z.; Cleverly, J.; Eamus, D. Evapotranspiration partitioning, stomatal conductance, and components of the water balance: A special case of a desert ecosystem in China. *J. Hydrol.* **2016**, *538*, 374–386. [CrossRef]
4. Zhao, W.; Ren, H.; Du, J.; Yang, R.; Yang, Q.; Liu, H. Thoughts and suggestions on oasis ecological construction and agricultural development in Hexi Corridor. *Bull. Chin. Acad. Sci. (Chin. Version)* **2023**, *38*, 424–434.
5. Wang, X.; Chen, X.; Ding, Q.; Zhao, X.; Wang, X.; Ma, Z.; Lian, J. Vegetation and soil environmental factor characteristics, and their relationship at different desertification stages: A case study in the Minqin desert-oasis ecotone. *Acta Ecol. Sin.* **2018**, *38*, 1569–1580. [CrossRef]
6. Zhaofeng, C.; Jianhui, Z.; Qiangqiang, W.; Shujuan, Z.; Dabiao, Z.; Baoli, F.; Jinnian, T.; Shizeng, L. Ecological Effects of Accumulated Sand-belts along the Oasis Fringe in Hexi of Gansu. *Anim. Husb. Feed Sci.* **2014**, *6*, 107.
7. Li, X.R.; Ma, F.Y.; Xiao, H.L.; Wang, X.P.; Kim, K.C. Long-term effects of revegetation on soil water content of sand dunes in arid region of Northern China. *J. Arid Environ.* **2004**, *57*, 1–16. [CrossRef]
8. Whitford, W.G.; Duval, B.D. *Ecology of Desert Systems*; Academic Press: Cambridge, MA, USA, 2019.
9. Wu, Y.; Zhou, H.; Zheng, X.J.; Li, Y.; Tang, L.S. Seasonal changes in the water use strategies of three co-occurring desert shrubs. *Hydrol. Process.* **2014**, *28*, 6265–6275.
10. D'Odorico, P.; Porporato, A.; Runyan, C.W. *Dryland Ecohydrology*; Springer: Berlin/Heidelberg, Germany, 2006; Volume 9.
11. Li, W.; Migliavacca, M.; Forkel, M.; Denissen, J.M.; Reichstein, M.; Yang, H.; Duveiller, G.; Weber, U.; Orth, R. Widespread increasing vegetation sensitivity to soil moisture. *Nat. Commun.* **2022**, *13*, 3959. [CrossRef] [PubMed]
12. Pan, S.; Pan, N.; Tian, H.; Friedlingstein, P.; Sitch, S.; Shi, H.; Arora, V.K.; Haverd, V.; Jain, A.K.; Kato, E. Evaluation of global terrestrial evapotranspiration using state-of-the-art approaches in remote sensing, machine learning and land surface modeling. *Hydrol. Earth Syst. Sci.* **2020**, *24*, 1485–1509.
13. Abed, M.; Imteaz, M.A.; Ahmed, A.N.; Huang, Y.F. Modelling monthly pan evaporation utilising Random Forest and deep learning algorithms. *Sci. Rep.* **2022**, *12*, 13132. [CrossRef] [PubMed]
14. Li, S.; Zhang, D.; Xing, Y.; Zhang, C.; Wang, Z.t.; Ma, R.; He, K.; Wang, P. Interannual dynamics and controlling factors of the ratio of actual to potential evapotranspiration across typical ecosystems within the Heihe River Basin. *Hydrol. Process.* **2024**, *38*, e15073. [CrossRef]
15. Wang, P.; Li, S.; Chen, Q.; Li, X.-Y.; Liu, S.; Wu, X.; Yang, X.; Xu, Z. A novel method for simulating the dynamics of the single and dual maize crop coefficients in an arid ecosystem. *Eur. J. Agron.* **2023**, *142*, 126688.
16. Xing, Y.; Wang, P.; Zhang, D.; Sun, H.; Li, S. Convergent control of soil temperature on seasonal carbon flux in Tibetan alpine meadows: An in-situ monitoring study. *Ecol. Indic.* **2023**, *156*, 111116. [CrossRef]
17. Wilson, K.; Goldstein, A.; Falge, E.; Aubinet, M.; Baldocchi, D.; Berbigier, P.; Bernhofer, C.; Ceulemans, R.; Dolman, H.; Field, C. Energy balance closure at FLUXNET sites. *Agric. For. Meteorol.* **2002**, *113*, 223–243. [CrossRef]
18. Li, X.; Gentine, P.; Lin, C.; Zhou, S.; Sun, Z.; Zheng, Y.; Liu, J.; Zheng, C. A simple and objective method to partition evapotranspiration into transpiration and evaporation at eddy-covariance sites. *Agric. For. Meteorol.* **2019**, *265*, 171–182. [CrossRef]
19. Liu, Y.; Zhang, Y.; Shan, N.; Zhang, Z.; Wei, Z. Global assessment of partitioning transpiration from evapotranspiration based on satellite solar-induced chlorophyll fluorescence data. *J. Hydrol.* **2022**, *612*, 128044. [CrossRef]

20. Zhao, W.; Hu, G.; Zhang, Z.; He, Z. Shielding effect of oasis-protection systems composed of various forms of wind break on sand fixation in an arid region: A case study in the Hexi Corridor, northwest China. *Ecol. Eng.* **2008**, *33*, 119–125. [CrossRef]
21. Carter, C.; Liang, S. Evaluation of ten machine learning methods for estimating terrestrial evapotranspiration from remote sensing. *Int. J. Appl. Earth Obs. Geoinf.* **2019**, *78*, 86–92. [CrossRef]
22. Amani, S.; Shafizadeh-Moghadam, H. A review of machine learning models and influential factors for estimating evapotranspiration using remote sensing and ground-based data. *Agric. Water Manag.* **2023**, *284*, 108324. [CrossRef]
23. Tian, F.; Qiu, G.; Lü, Y.; Yang, Y.; Xiong, Y. Use of high-resolution thermal infrared remote sensing and "three-temperature model" for transpiration monitoring in arid inland river catchment. *J. Hydrol.* **2014**, *515*, 307–315.
24. Morgan, B.E.; Caylor, K.K. Estimating Fine-Scale Transpiration From UAV-Derived Thermal Imagery and Atmospheric Profiles. *Water Resour. Res.* **2023**, *59*, e2023WR035251.
25. Meerdink, S.K.; Roberts, D.A.; King, J.Y.; Roth, K.L.; Gader, P.D.; Caylor, K.K. Using hyperspectral and thermal imagery to monitor stress of Southern California plant species during the 2013–2015 drought. *ISPRS J. Photogramm. Remote Sens.* **2025**, *220*, 580–592. [CrossRef]
26. Qiu, G.Y.; Momii, K.; Yano, T. Estimation of plant transpiration by imitation leaf temperature theoretical consideration and field verification (I). *Trans. Jpn. Soc. Irrig. Drain. Reclam. Eng.* **1996**, *1996*, 401–410, a401.
27. Xiong, Y.J.; Zhao, S.H.; Tian, F.; Qiu, G.Y. An evapotranspiration product for arid regions based on the three-temperature model and thermal remote sensing. *J. Hydrol.* **2015**, *530*, 392–404. [CrossRef]
28. Wang, P.; Zhang, D.; Xing, Y.; Li, X.-Y.; Qiu, G.; Wu, X.; Sun, H.; Xiong, Y.; Wang, L. Integrating temperature gradient-based 3T and resistance-based models for simulating evapotranspiration and its components. *J. Hydrol.* **2023**, *620*, 129459.
29. Feng, L.; Liu, Y.; Zhou, Y.; Yang, S. A UAV-derived thermal infrared remote sensing three-temperature model and estimation of various vegetation evapotranspiration in urban micro-environments. *Urban For. Urban Green.* **2022**, *69*, 127495.
30. Lu, S.; Zhang, T.; Tian, F. Evaluation of crop water status and vegetation dynamics for alternate partial root-zone drip irrigation of alfalfa: Observation with an UAV thermal infrared imagery. *Front. Environ. Sci.* **2022**, *10*, 791982. [CrossRef]
31. Yan, C.; Xiang, J.; Qin, L.; Wang, B.; Shi, Z.; Xiao, W.; Hayat, M.; Qiu, G.Y. High temporal and spatial resolution characteristics of evaporation, transpiration, and evapotranspiration from a subalpine wetland by an advanced UAV technology. *J. Hydrol.* **2023**, *623*, 129748.
32. Qiu, G.Y.; Ben-Asher, J.; Yano, T.; Momii, K. Estimation of soil evaporation using the differential temperature method. *Soil Sci. Soc. Am. J.* **1999**, *63*, 1608–1614. [CrossRef]
33. Liang, S. Narrowband to broadband conversions of land surface albedo I: Algorithms. *Remote Sens. Environ.* **2001**, *76*, 213–238. [CrossRef]
34. Sobrino, J.A.; Jiménez-Muñoz, J.C.; Paolini, L. Land surface temperature retrieval from LANDSAT TM 5. *Remote Sens. Environ.* **2004**, *90*, 434–440. [CrossRef]
35. Swinbank, W.C. Long-wave radiation from clear skies. *Q. J. R. Meteorol. Soc.* **1963**, *89*, 339–348. [CrossRef]
36. Su, Z. The Surface Energy Balance System (SEBS) for estimation of turbulent heat fluxes. *Hydrol. Earth Syst. Sci.* **2002**, *6*, 85–100. [CrossRef]
37. Kustas, W.P.; Daughtry, C.S.T. Estimation of the soil heat flux/net radiation ratio from spectral data. *Agric. For. Meteorol.* **1990**, *49*, 205–223. [CrossRef]
38. Monteith, J.; Unsworth, M. *Principles of Environmental Physics: Plants, Animals, and the Atmosphere*; Academic Press: Cambridge, MA, USA, 2013.
39. Jackson, R.D.; Hatfield, J.L.; Reginato, R.; Idso, S.; Pinter, P., Jr. Estimation of daily evapotranspiration from one time-of-day measurements. *Agric. Water Manag.* **1983**, *7*, 351–362.
40. Bastiaanssen, W.G.; Menenti, M.; Feddes, R.; Holtslag, A. A remote sensing surface energy balance algorithm for land (SEBAL). 1. Formulation. *J. Hydrol.* **1998**, *212*, 198–212. [CrossRef]
41. Wang, P.; Yamanaka, T. Application of a two-source model for partitioning evapotranspiration and assessing its controls in temperate grasslands in central Japan. *Ecohydrology* **2014**, *7*, 345–353.
42. Sandholt, I.; Rasmussen, K.; Andersen, J. A simple interpretation of the surface temperature/vegetation index space for assessment of surface moisture status. *Remote Sens. Environ.* **2002**, *79*, 213–224. [CrossRef]
43. Aboutalebi, M.; Torres-Rua, A.F.; Kustas, W.P.; Nieto, H.; Coopmans, C.; McKee, M. Assessment of different methods for shadow detection in high-resolution optical imagery and evaluation of shadow impact on calculation of NDVI, and evapotranspiration. *Irrig. Sci.* **2019**, *37*, 407–429.
44. Lu, S.; Xuan, J.; Zhang, T.; Bai, X.; Tian, F.; Ortega-Farias, S. Effect of the shadow pixels on evapotranspiration inversion of vineyard: A high-resolution UAV-based and ground-based remote sensing measurements. *Remote Sens.* **2022**, *14*, 2259.
45. Timmermans, W.J.; Kustas, W.P.; Anderson, M.C.; French, A.N. An intercomparison of the surface energy balance algorithm for land (SEBAL) and the two-source energy balance (TSEB) modeling schemes. *Remote Sens. Environ.* **2007**, *108*, 369–384. [CrossRef]
46. Camillo, P.J.; Gurney, R.J. A resistance parameter for bare-soil evaporation models. *Soil Sci.* **1986**, *141*, 95–105. [CrossRef]

47. Shen, Q.; Gao, G.; Fu, B.; Lü, Y. Responses of shelterbelt stand transpiration to drought and groundwater variations in an arid inland river basin of Northwest China. *J. Hydrol.* **2015**, *531*, 738–748. [CrossRef]
48. Chang, X.; Zhao, W.; Zhang, Z.; Su, Y. Sap flow and tree conductance of shelter-belt in arid region of China. *Agric. For. Meteorol.* **2006**, *138*, 132–141. [CrossRef]
49. Shen, Q.; Gao, G.; Fu, B.; Lü, Y. Sap flow and water use sources of shelter-belt trees in an arid inland river basin of Northwest China. *Ecohydrology* **2015**, *8*, 1446–1458. [CrossRef]
50. Hao, X.M.; Chen, Y.N.; Guo, B.; Ma, J.X. Hydraulic redistribution of soil water in *Populus euphratica* Oliv. in a central Asian desert riparian forest. *Ecohydrology* **2013**, *6*, 974–983.
51. Ward, D.; Wiegand, K.; Getzin, S. Walter's two-layer hypothesis revisited: Back to the roots! *Oecologia* **2013**, *172*, 617–630. [PubMed]
52. Wu, X.; Zheng, X.-J.; Li, Y.; Xu, G.-Q. Varying responses of two Haloxylon species to extreme drought and groundwater depth. *Environ. Exp. Bot.* **2019**, *158*, 63–72. [CrossRef]
53. Moreno-Gutiérrez, C.; Dawson, T.E.; Nicolás, E.; Querejeta, J.I. Isotopes reveal contrasting water use strategies among coexisting plant species in a Mediterranean ecosystem. *New Phytol.* **2012**, *196*, 489–496. [CrossRef] [PubMed]
54. Yang, B.; Wen, X.; Sun, X. Seasonal variations in depth of water uptake for a subtropical coniferous plantation subjected to drought in an East Asian monsoon region. *Agric. For. Meteorol.* **2015**, *201*, 218–228. [CrossRef]
55. Fort, F.; Volaire, F.; Guilioni, L.; Barkaoui, K.; Navas, M.L.; Roumet, C. Root traits are related to plant water-use among rangeland Mediterranean species. *Funct. Ecol.* **2017**, *31*, 1700–1709.
56. Wang, P.; Li, X.Y.; Wang, L.; Wu, X.; Hu, X.; Fan, Y.; Tong, Y. Divergent evapotranspiration partition dynamics between shrubs and grasses in a shrub-encroached steppe ecosystem. *New Phytol.* **2018**, *219*, 1325–1337. [PubMed]

Disclaimer/Publisher's Note: The statements, opinions and data contained in all publications are solely those of the individual author(s) and contributor(s) and not of MDPI and/or the editor(s). MDPI and/or the editor(s) disclaim responsibility for any injury to people or property resulting from any ideas, methods, instructions or products referred to in the content.